Supporting Information: Multicone Diamond Waveguides for Nanoscale Quantum Sensing

Tianqi Zhu,[†] Jan Rhensius,[‡] Konstantin Herb,[†] Viraj Damle,[‡] Gabriel Puebla-Hellmann,[‡] Christian L. Degen,[*,†] and Erika Janitz[*,¶]

[†]*Department of Physics, ETH Zürich, Otto-Stern-Weg 1, 8093 Zürich, Switzerland*

[‡]*QZabre LLC, Regina-Kägi-Strasse 11, 8050 Zürich, Switzerland*

[¶]*Department of Electrical and Software Engineering, University of Calgary, 2500 University Drive NW, Calgary AB Canada, T2N 1N4*

E-mail: degenc@ethz.ch; erika.janitz@ucalgary.ca

Wavelength-Dependent Far-Field Emission Intensity

Figure 2b of the main text shows the simulated far-field intensities resulting from NV emission within a 1-μm-tall SC, 5-μm-tall SC, and 5-μm-tall MC. To gain further intuition for the wavelength-dependent device performance, we also plot the far-field intensities for monochromatic emission at 650, 721, and 800 nm (Fig. S1). The MC device exhibits superior performance in terms of collimation and directionality at all three wavelengths.

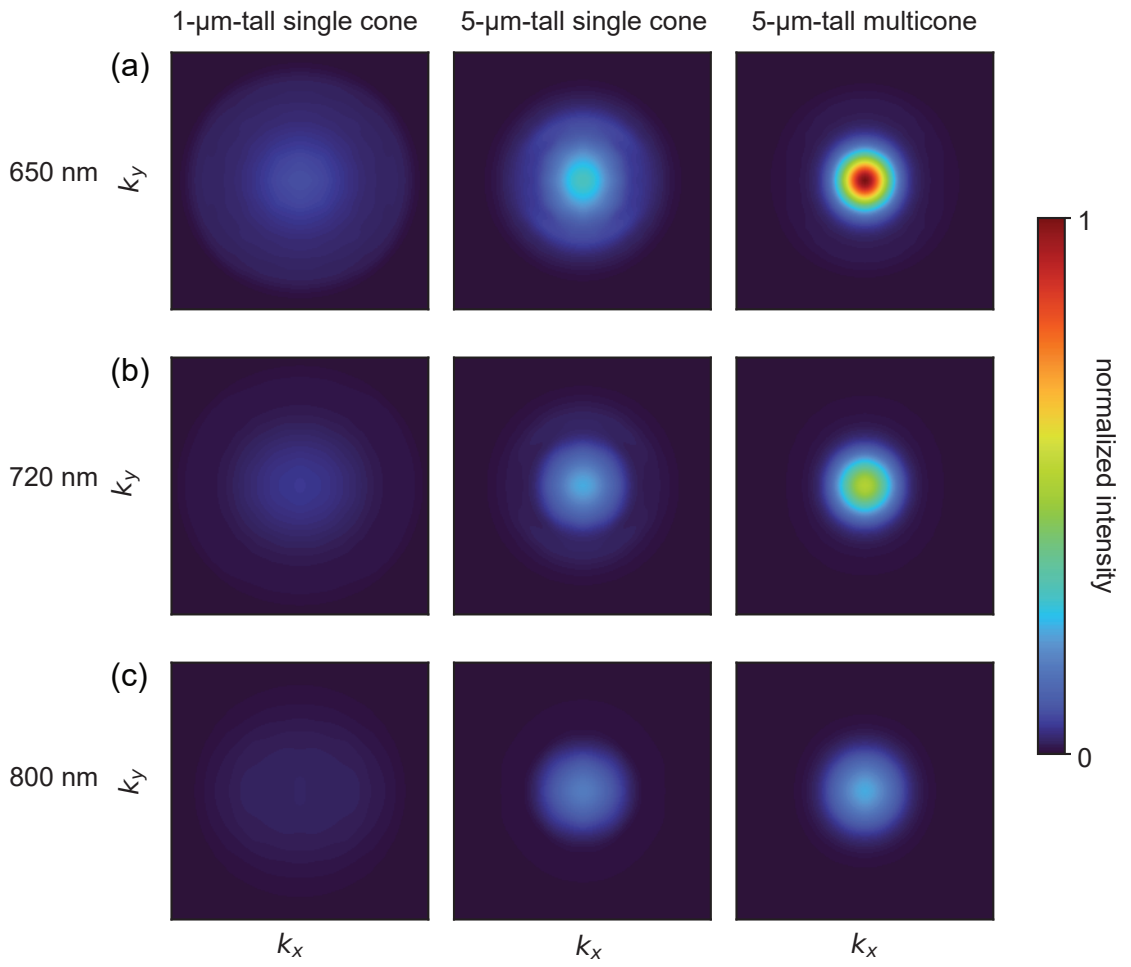

Figure S1: Simulated far-field intensities for 1-μm-tall single-cone, 5-μm-tall single-cone, and 5-μm-tall multicone devices with monochromatic emission at a) 650 nm, b) 721 nm, and c) 800 nm.

Diamond Fabrication

To ensure consistent material properties, all devices were created from the same electronic-grade diamond plate ((100)-cut, $2 \times 2 \times 0.5$ mm, Element 6), which was subsequently diced into 20-μm-thick membranes (surface roughness ≈ 0.8 nm-rms, Almax easyLab). An inductively coupled plasma reactive-ion etching (ICP RIE, Oxford Instruments PlasmaPro 100) recipe was used to condition the diamond surface before NV centers were created. This recipe removes $\approx$ 6 μm of material to smooth the diamond surface and relieve polishing strain (Tab. S1).

Table S1: Diamond ICP RIE surface conditioning recipe.

Step	Process	Duration (min)
1	Ar (25 sccm) + Cl_2 (40 sccm)	60
2	Ar (25 sccm) + Cl_2 (40 sccm)	5
3	O_2 (30 sccm)	10
4	3× repeat steps 2 + 3	

Next, 5 ± 2 nm-deep[1] NV centers were created using ion implantation (Cutting Edge Ions, 3 keV, 8×10^9 ions/cm^3) and subsequent high-vacuum annealing (880°C for 2 hours, P$< 3 \times 10^{-8}$ mbar).

Pillars were lithographically defined using three layers of electron-beam resist, including a layer of PMGI (SF-8, Kayaku Advanced Materials) followed by 950K PMMA (4.5% in anisole, Allresist) for bilayer liftoff, and a final layer of Espacer 300Z to avoid charging (Showa Denko). Following lithography (Raith 150, 20 kV, 20 µm aperture), the resist was developed using a sequence of deionized (DI) water, MIBK, isopropanol, AZ 726 MIF, and DI water. As a mask, a 200-nm-thick layer of aluminum was deposited by electron-beam evaporation (Plassys MEB550S) followed by liftoff in warm DMSO for pillars 1-3. In contrast, a 320-nm-thick aluminum layer was deposited for pillar 4.

Subsequently, pillars 1, 2, and 3 (see Fig. 3 in main text) were defined using an O_2-plasma recipe with intermittent SF_6 plasma to avoid micromasking (Tabs. S2, S3, and S4). These recipes were terminated once the aluminum mask eroded to a radius of $\approx$ 150 nm (determined using a scanning electron microscope).

Table S2: ICP RIE recipe for pillar 1.

Step	Process	Duration (min)
1	SF_6 (30 sccm)	0.5
2	SF_6 (30 sccm)	0.5
3	O_2 (50 sccm)	8
4	SF_6 (30 sccm)	0.5
5	SF_6 (30 sccm)	0.5
6	O_2 (50 sccm)	2

Table S3: ICP RIE recipe for pillar 2.

Step	Process	Duration (min)
1	SF_6 (Gas flow: 30 sccm)	0.5
2	SF_6 (Gas flow: 30 sccm)	0.5
3	O_2 (Gas flow: 50 sccm)	8
4	2× repeat steps 2 + 3	

Table S4: ICP RIE recipe for pillar 3.

Step	Process	Duration
1	SF_6 (30 sccm)	0.5
2	SF_6 (30 sccm)	0.5
3	$O2_2$ (50 sccm)	8
4	4× repeat steps 2 + 3	
5	SF_6 (30 sccm)	0.5
6	SF_6 (30 sccm)	0.5
7	O_2 (50 sccm)	2

In contrast, pillar 4 (see Fig. 3 in the main text) was first etched with the same recipe as pillars 1-3 until approximately 4.5 µm of material was removed. Next, a mixture of SF_6 and O_2 was used (Tab. S5) to etch an additional 0.5 µm, resulting in a shallow sidewall angle near the top of the device.

Table S5: ICP RIE recipe for pillar 4.

Step	Process	Duration (min)
1	SF_6 (30 sccm)	0.5
2	SF_6 (30 sccm)	0.5
3	O_2 (50 sccm)	10.5
4	4× repeat steps 2 + 3	
5	SF_6 (10 sccm) + O_2 (40 sccm)	9

Experimental Setup

Nanopillars are characterized using the confocal microscope illustrated in Fig. S2. We excite NV centers using a home-built 520-nm excitation laser reflected at a dichroic beamsplitter (Semrock SEM-FF526). Subsequently, the beam is scanned using galvo mirrors onto the

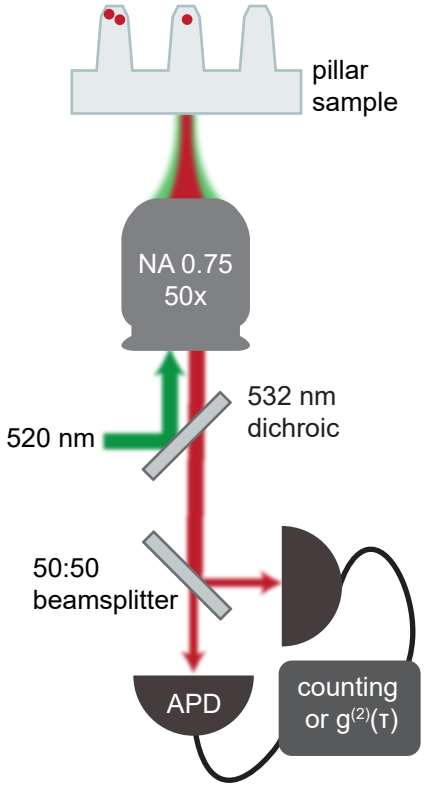

Figure S2: A simplified schematic of the confocal microscope.

back of an objective lens (Mitutoyo Plan Apo HR 50×, NA = 0.75) and is focused onto the sample.

Fluorescence is collected through the objective, transmitted through the dichroic, spectrally filtered (Semrock SEM-FF01-709/167), split by a 50:50 beamsplitter, and coupled into two optical fibers (SMF28). These fibers exhibit multimode operation over the NV emission spectrum; consequently, we assume all light within the experimental NA is collected. Finally, collected photons are sent to fiber-coupled avalanche photodiodes (APDs, Laser Components COUNT®), and the recorded counts are either summed to obtain the total NV fluorescence or used as inputs for a time-correlated single-photon-counting system (TCSPC, PicoQuant Picoharp 300).

In contrast, back-focal-plane imaging uses a flip mirror in the collection path (these measurements were conducted using a different NA=0.95 objective). The emission is subsequently focused onto an electron-multiplying charge-coupled device (EMCCD, Andor Luca R) using a lens.

Emitter Displacement

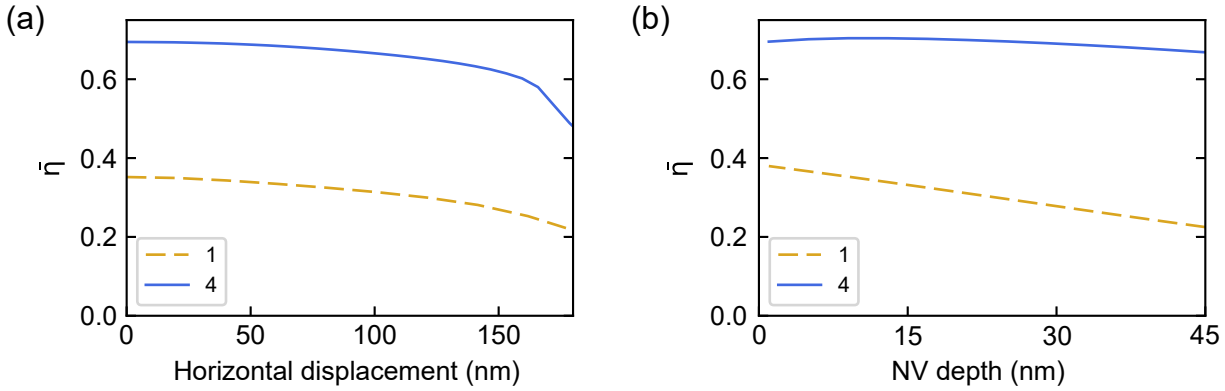

Figure S3: Simulated collection efficiencies for pillars 1 and 4 as a function of NV-center position. (a) Impact of horizontal displacement δ (d=5 nm and $R_{\text{top}} = 180$ nm). (b) Impact of vertical position d (δ=0 nm and $R_{\text{top}} = 180$ nm)

We simulate the impact of horizontal displacement (δ) and vertical NV position (d) on

collection efficiency for pillar 1 (SC) and 4 (MC) devices (Fig. S3). We observe a relatively minor reduction ($< 30\%$ in $\bar{\eta}$) as the NV moves from the center to the edge of the device in both geometries (Fig. S3a). In addition, vertical displacements of up to 40 nm (expected depth $d = 5 \pm 2$ nm) reduce $\bar{\eta}$ by less than a factor of two for the pillar 1 geometry and have very little impact on the MC. Consequently, for simplicity, we model all emitters as centered within the pillar ($\delta = 0$) and at a depth of $d = 5$ nm.

Single-Photon Emission

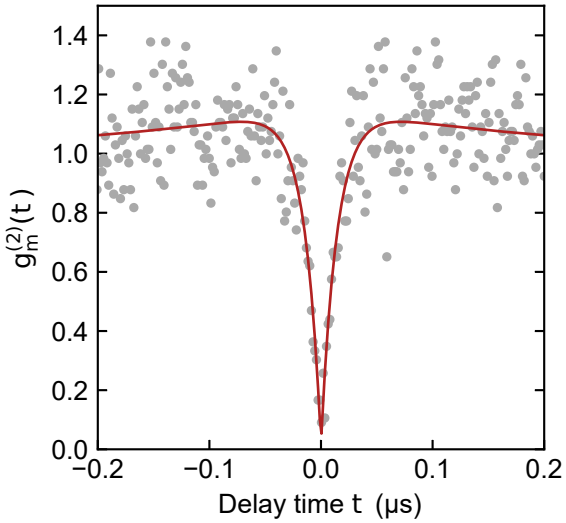

Figure S4: Second-order coherence measurement (grey dots) and fit to Eq. 1 (red line) for a representative pillar 4 device with $g_m^{(2)}(0) = 0.02 \pm 0.06$. Here, we obtain $\rho = 0.99 \pm 0.03$, $\beta = 0.17 \pm 0.03$, $\tau_1 = 14.5 \pm 1.3$ ns, and $\tau_2 = 210 \pm 40$ ns.

We identify pillars containing single NV centers using second-order coherence measurements ($g_m^{(2)}(\tau)$, Fig. S4) obtained with the TCSPC. These data are fit assuming a Poissonian background parameterized by $\rho = S/(S + B)$, where S is the signal from the NV center and B is the background,[2] yielding

$$g_m^{(2)}(t) = g^{(2)}(t)\rho^2 + 1 - \rho^2, \tag{1}$$

where

$$g^{(2)}(t) = 1 - (1+\beta)e^{-|t|/\tau_1} + \beta e^{-|t|/\tau_2}. \tag{2}$$

Here, β, τ_1, and τ_2 are fit parameters related to the excitation and decay rates.[2] Single photon emission is unequivocally demonstrated for $g_m^{(2)}(0) < 0.5$; consequently, we select emitters where the sum of the average and standard deviation does not exceed this value.

Back-Focal-Plane Imaging

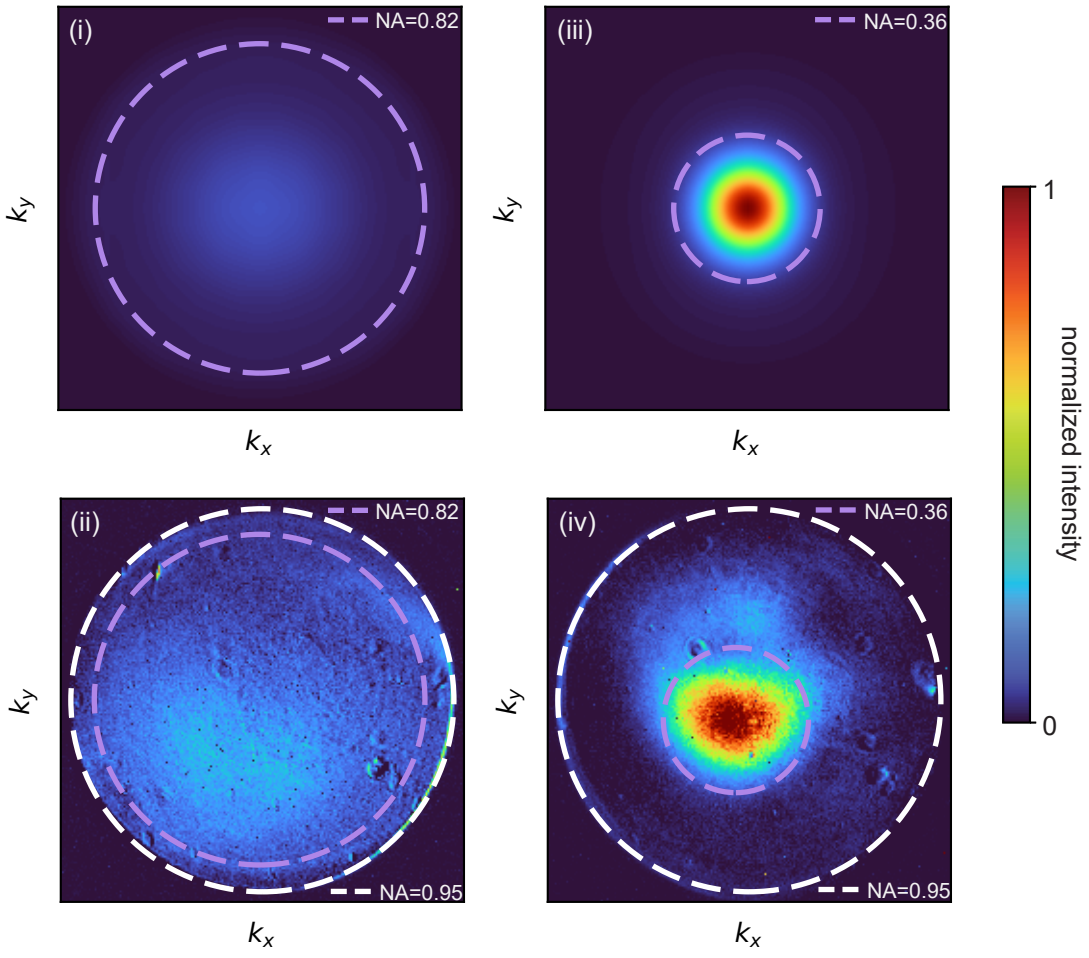

Figure S5: (i) Far-field intensity simulation for a 1-µm-tall single cone. (ii) Back-focal-plane image of a pillar 1 device. (ii) Far-field intensity simulation for a 5-µm-tall multicone. (iv) Back-focal-plane image of a pillar 4 device. Color bars are normalized to the peak intensities obtained for the multicone structures (iii and iv).

We have conducted back-focal-plane (BFP) imaging (Fig. S5) to experimentally validate the simulation predictions in Fig. 2 of the main text. Specifically, we have measured pillar 1 (Fig. S5(ii)) and pillar 4 (Fig. S5(iv)) devices, which can be most closely compared against the far-field simulations for the 1-μm-tall single cone (Fig. S5(i)) and 5-μm-tall multicone (Fig. S5(iii)), respectively. As in Fig. 2b of the main text, we overlay dashed purple circles in the simulations (top row) corresponding to $\mathrm{NA}_{0.80}$, the numerical aperture at which 80% of light is collected for NA=1. This highlights the enhanced collimation achieved for a tall multicone structure. For comparison, we overlay the corresponding BFP images with the same circles, including some lateral offset to account for setup misalignment. These images show excellent qualitative agreement with the far-field images, validating our simulation model.

Rabi Measurement

We estimate the optical contrast between spin states for a representative pillar 4 device by performing power-dependent Rabi measurements (Fig. S6). Specifically, we fit the first fringe of the oscillation to

$$R(t) = \frac{C\, e^{-t/\tau}}{2} \cos(2\pi f t + \psi) + A, \tag{3}$$

where C is the spin contrast, τ is the contrast decay constant, f is the Rabi frequency, ψ is a phase offset, and A is the measurement offset.

We observed instability in the laser output power at low power settings ($P_{\mathrm{set}} \leq 1$ mW); consequently, we label each measurement with the programmed power and integrate the photon counts per measurement α_0 explicitly in calculating the spin-readout SNR (details in main text).

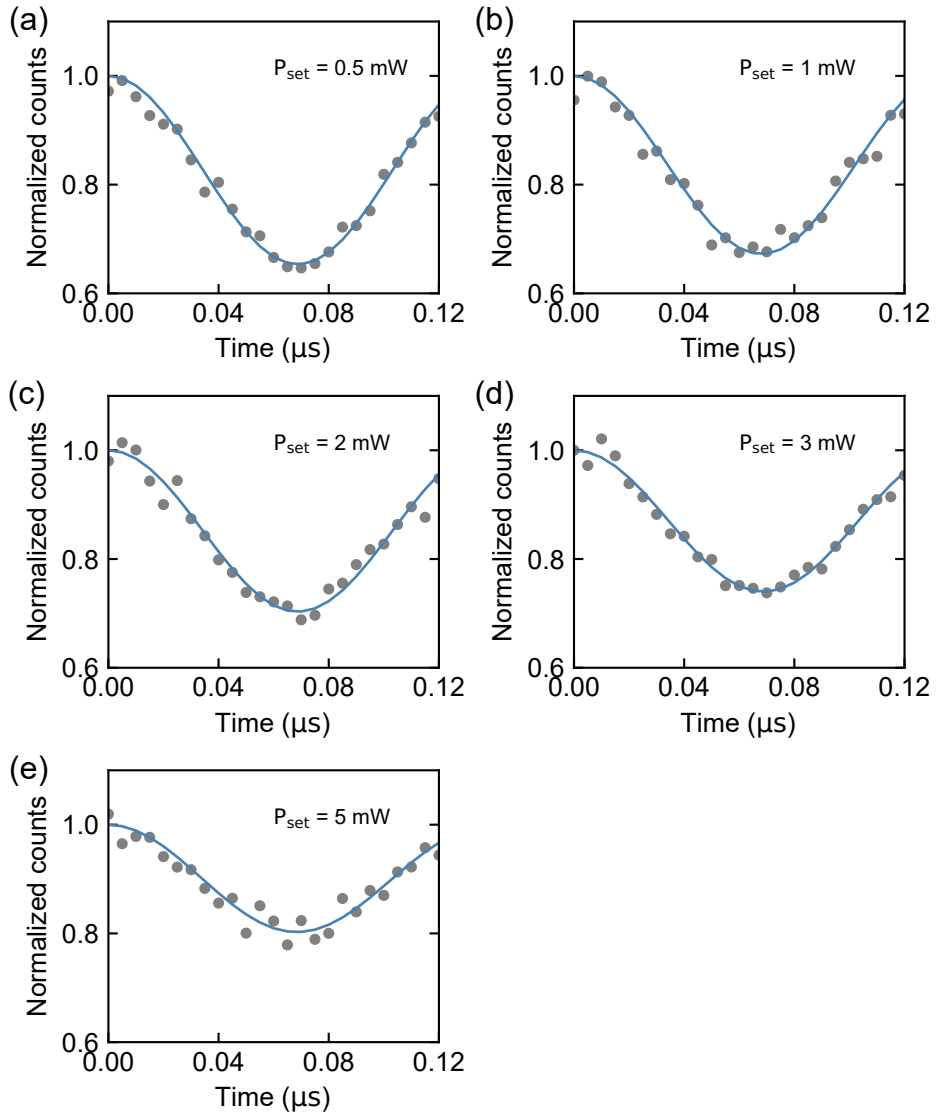

Figure S6: Rabi oscillation measurements (grey dots) at different laser powers for a representative pillar 4 device. Fits to Eq. 3 yield contrast values of a) $C = 34.7 \pm 0.9\%$, b) $C = 32.8 \pm 1.1\%$, c) $C = 29.7 \pm 1.0\%$, d) $C = 26.0 \pm 0.7\%$, and e) $C = 20.1 \pm 1.0\%$.

References

(1) Ziegler, J. F.; Ziegler, M. D.; Biersack, J. P. SRIM–The Stopping and Range of Ions in Matter (2010). *Nucl. Instrum. Methods Phys. Res. Sect. B Beam Interact. Mater. At.* **2010**, *268*, 1818–1823.

(2) Brouri, R.; Beveratos, A.; Poizat, J.-P.; Grangier, P. Photon Antibunching in the Fluorescence of Individual Color Centers in Diamond. *Opt. Lett.* **2000**, *25*, 1294–1296.